Modeling and Analysis of VIV-Galloping Coupled Piezoelectric Energy Harvester Shunted to SECE Interface Circuit

Ye Zhang, Yawei Wang, Junlei Wang, and Guobiao Hu

***Abstract*—This article investigates the performance enhancement of flow-induced vibration piezoelectric energy harvesters through the coupling of vortex-induced vibration (VIV) and galloping. Strips are attached to the surface of cylindrical bluff bodies to induce VIV-galloping coupling, resulting in VIV-galloping coupled piezoelectric energy harvesters (VGPEHs). As voltage outputs from VGPEHs require regulation by interface circuits for practical use, an equivalent circuit model (ECM) is proposed to integrate complex circuits into the analysis. The vortex-induced vibration is described by the wake oscillator equation, with aerodynamic force coefficients derived from computational fluid dynamics simulations. The ECM method is validated through wind tunnel experiments, and further studies explore the power output of the VGPEH shunted to ac, dc, and self-powered synchronous electric charge extraction (SP-SECE) circuits. Both experimental and ECM simulation results show that the SP-SECE circuit provides more stable, though lower, output power across a wide resistance range than the dc circuit. Simulation and limited power theory suggest that the SP-SECE circuit outperforms the dc circuit under weak coupling conditions, but the VGPEH prototype operates under strong coupling conditions. From a practical perspective, a strongly coupled harvester is more cost-effective than a weakly coupled harvester that relies on a complex SP-SECE circuit for power-boosting.**

***Index Terms*—Equivalent circuit model (ECM), interface circuit, piezoelectric energy harvesting, vortex-induced vibration (VIV)-galloping coupled vibration.**

NOMENCLATURE

Variables	*Explanation*
D, H	Diameter and height of bluff body.
α_1, β_1, h_1	Installation angle, coverage angle, height of strip.
L_p, W_p, T_p	Length, width and thickness of PZT-5 patch.
L_b, W_b, T_b	Length, width and thickness of cantilever beam.
$\ddot{\eta}(t)$, $\dot{\eta}(t)$, $\eta(t)$	Modal acceleration, modal velocity, modal coordinate of bluff body.
ω_n, ζ	The natural angular frequency and the damping ratio of VGPEH.
λ	The damping ratio of the Van der Pol wake oscillator equation.
γ, A_i	The constant related to the aspect ratio of the bluff body and the galloping force coefficient.
M_{eff}, C_{eff}, K_{eff}	Equivalent mass, damping and stiffness of VGPEH.
θ, C_p	Electromechanical coupling coefficient and internal capacitance of VGPEH.
$f_a(t)$, $C_{Fz}(t)$, $C_L(t)$	The aerodynamic force, the aerodynamic force coefficient and the lift force coefficient.
C_D, f	The averaged drag force coefficient and the VIV-galloping coupled coefficient.
$\ddot{z}(t)$, $\dot{z}(t)$, $z(t)$	Acceleration, velocity and displacement of the bluff body.
$\ddot{q}(t)$, $\dot{q}(t)$, $q(t)$	Relevant wake variables of wake oscillator model.
ω_V, C_{L0}	The angular vortex shedding frequency and the amplitude of the lift force coefficient.
L_1, C_1, R_1	The corresponding analogy parameter of M_{eff}, C_{eff}, K_{eff}.
L_2, C_2, R_2	The corresponding analogy parameter in wake oscillator model.
$\ddot{Q}_1(t)$, $\dot{Q}_1(t)$, $Q_1(t)$	The corresponding equivalent parameter of $\ddot{z}(t)$, $\dot{z}(t)$, $z(t)$.
$\ddot{Q}_2(t)$, $\dot{Q}_2(t)$, $Q_2(t)$	The corresponding equivalent parameter of $\ddot{q}(t)$, $\dot{q}(t)$, $q(t)$.

Received 22 January 2025; revised 1 May 2025 and 9 July 2025; accepted 20 August 2025. Recommended by Technical Editor A. Trejos and Senior Editor H. Fujimoto. This work was supported in part by the National Natural Science Foundation of China under Grant 52305135, and Grant 52277227, in part by the Guangdong Provincial Key Lab of Integrated Communication, Sensing and Computation for Ubiquitous Internet of Things under Grant 2023B1212010007, in part by the Guangzhou Municipal Science and Technology Project under Grant 2023A03J0011, and in part by the Guangzhou Municipal Key Laboratory on Future Networked Systems under Grant 024A03J0623. *(Corresponding authors: Junlei Wang; Guobiao Hu.)*

Ye Zhang, Yawei Wang, and Guobiao Hu are with the Thrust of Internet of Things, The Hong Kong University of Science and Technology (Guangzhou), Guangzhou 511400, China (e-mail: m19544542711@163.com; ywang642@connect.hkust-gz.edu.cn; guobiaohu@hkust-gz.edu.cn).

Junlei Wang is with the School of Mechanical and Power Engineering, Zhengzhou University, Zhengzhou 450000, China (e-mail: jlwang@zzu.edu.cn).

Color versions of one or more figures in this article are available at https://doi.org/10.1109/TMECH.2025.3603589.

Digital Object Identifier 10.1109/TMECH.2025.3603589

$V(t)$, $\dot{V}(t)$	Voltage variable and its first derivative.
I_1(iin), I_2(iin)	The current variables in ECM.

I. Introduction

WIND-INDUCED vibration (WIV) phenomena arise from fluid-structure interactions. Energy carried by fluids can be harnessed and converted into structural oscillations through the exploitation of WIV phenomena [1]. Converting such vibrations into electricity has garnered significant attention and has been widely studied in recent years [2]. Among various WIV phenomena, vortex-induced vibration (VIV) and galloping are the most extensively utilized for energy harvesting, primarily due to their occurrence at low wind speeds [3]. Compared to galloping, VIV typically occurs at lower wind speeds, making VIV-based energy harvesting ideal for applications where wind is not consistently strong. In contrast, galloping generates larger amplitude oscillations, particularly when the wind speed is high enough to trigger this instability. As a result, galloping energy harvesting is especially effective in high-wind conditions [4]. WIV serves as the first-stage conversion mechanism, transforming fluid energy into vibrations [5]. Piezoelectric transducers are often used for the second-stage energy conversion, which transforms vibrations into electricity due to their low cost, easy integration, and high power density [6], [7].

To enhance the performance of flow-induced vibration piezoelectric energy harvesters, methods, such as etching grooves on the surfaces of bluff bodies and introducing magnetic forces, have been proposed from the perspective of optimizing mechanical dynamics. Xing et al. [8] introduced different surface protrusions on the bluff body of a galloping piezoelectric energy harvester (GPEH). Their findings revealed that the vibration mode varied with the type of protrusions, and the output power increased by 157.48% when using elliptical surface protrusions. Li et al. [9] integrated magnetic nonlinear forces into the design of a GPEH, with experimental results indicating a reduction in galloping onset speed and enhanced performance attributed to the softening effect. Since, as above-mentioned, VIV is more effective at lower wind speeds and galloping excels at higher wind speeds, coupling these two phenomena allows for enhanced operational efficiency across a wider range of wind speeds. Based on this idea, Wang et al. [10] developed a hybrid wind energy harvester by coupling VIV and galloping, resulting in a reduced cut-in wind speed. Yang et al. [11] developed a theoretical model for a VIV-galloping coupled piezoelectric energy harvester (VGPEH) and validated it via a wind tunnel experiment.

On the other hand, researchers explored improving energy harvesting performance through the design and application of advanced interface circuits, these early circuit designs made significant contributions to enhancing the power outputs of piezoelectric energy harvesters and boosting their efficiencies [12], [13], [14]. To incorporate circuits into the modeling, Tang et al. [15] first proposed an equivalent circuit model (ECM) to represent a GPEH, where the mechanical and aerodynamic parameters are replaced by analogous electrical elements. Based on the developed ECM, Zhao et al. [16] further considered the synergy of the GPEH and a synchronized switch harvesting interface (SSHI) circuit. Using a similar approach, Jia et al. [17] built an ECM for a vortex-induced vibration piezoelectric energy harvester (VIVPEH) and studied the influences of simple rectifier circuits on the output performance. Priore et al. [18] extended the method to analyze a VGPEH under ac, dc, and SSHI circuit conditions. A parametric study was conducted to optimize the VGPEH. However, due to the complexity of the aerodynamic interactions, they employed Simulink to solve the underlying ODEs directly, bypassing the need to represent the mechanical system as an equivalent circuit. More recently, Wang et al. [19] introduced nonlinear magnetic forces into VIV and developed a general ECM for it. Based on that model, they investigated the influences of different circuits on the performance of the nonlinear VIVPEH.

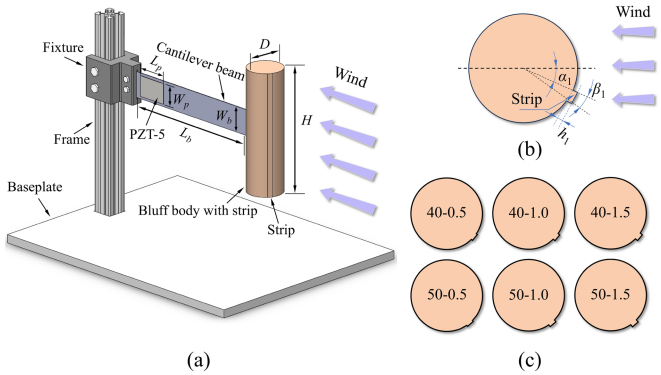

Fig. 1. (a) Mechanical structure of the proposed VIV-galloping coupled piezoelectric energy harvester (VGPEH). (b) Schematic of the strip and its design parameters. (c) Six bluff bodies with different strip configurations.

The literature review reveals that limited research has been conducted on developing equivalent circuit models for VIV-galloping coupled piezoelectric energy harvesters, primarily due to the mathematical complexity of the problem. Therefore, the effects of nonlinear interface circuits on their performance remain unexplored. To address this research gap, based on mechanical-electrical analogies, this study introduces a general ECM approach for modeling VGPEHs and validates it through wind tunnel experiments. Furthermore, the effects of different interface circuits (ac, dc, and SP-SECE) on the output responses of the VGPEH are simulated and analyzed. Based on the developed ECM, the conditions under which the SP-SECE circuit outperforms traditional circuits are identified.

II. VIV-Galloping Coupled Piezoelectric Energy Harvester

Fig. 1(a) shows the structure of the proposed VGPEH. The bluff body with dimensions of $D \times H$ is fixed at one end of the cantilever beam, the PZT-5 patch with dimensions of $L_p \times W_p \times T_p$ is boned near the clamped end of the cantilever beam, and the VGPEH is mounted on the frame. The baseplate serves to isolate vibrations. As shown in Fig. 1(b), a strip is attached to the surface of the cylinder, with an installation angle of α_1 to the incoming flow U, the coverage angle is β_1, and the

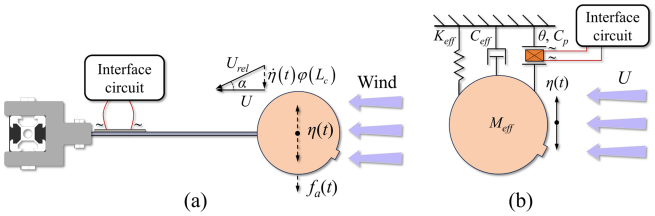

Fig. 2. (a) Top view of the VGPEH. (b) Lumped parameter model of the SDOF VGPEH.

height is h_1. The strip has the same length as the bluff body. This technique has been applied in many FIV studies as it can help induce the galloping phenomenon and lead to a high amplitude vibration at high flow speeds [20], [21], [22]. Numerous studies have successfully achieved VIV-galloping coupled vibration using different kinds of strips [23], [24], [25]. Following the previous configuration, in this study, the installation angle α_1 is set to be 40° or 50°. The coverage angle β_1 is fixed at 15.7°, h_1 varies from 0.5 to 1.5 mm. Finally, as illustrated in Fig. 1(c), six bluff bodies with different α_1 and h_1 have been prepared, designated as α_1–h_1: 40–0.5, 40–1.0, 40–1.5, 50–0.5, 50–1.0, and 50–1.5. In the wind tunnel experiment, the cylinder and cuboid bluff bodies are also tested and are referred to as the baseline models.

III. Theoretical Model For VIV-Galloping Coupled Piezoelectric Energy Harvester

A. Single-Degree-of-Freedom Lumped Parameter Model

Traditional galloping and VIVPEHs activate fundamental resonances at low wind speeds, leading researchers to often simplify them as single-degree-of-freedom (SDOF) models [26], [27]. As with other systems, for the VGPEH, as illustrated in Fig. 2, only its fundamental resonance is included in the modeling [28]. The corresponding governing equation in the modal coordinate form can be derived as follows [29]:

$$\ddot{\eta}(t)+2\omega_n\zeta\dot{\eta}(t)+\omega_n^2\eta(t)+\Theta V(t)=f_a(t) \tag{1}$$

$$f_a(t)=-\frac{1}{2}\rho U^2 DH\varphi(L_c)C_{Fz}(t) \tag{2}$$

$$C_{Fz}(t)=[C_L(t)+C_D\tan\alpha]\sec\alpha \tag{3}$$

where U is the wind speed, $C_{Fz}(t)$ is the aerodynamic force coefficient, C_D is the averaged drag force coefficient, $\varphi(L_c)$ is the modal shape of the fundamental resonance. α is the attack angle and $\tan\alpha=\dot{\eta}(t)\varphi(Lc)/U$ in Fig. 2(a), it can be assumed that $\sec\alpha\approx 1$ because $\dot{\eta}(t)$ is much smaller than U. The lift force coefficient $C_L(t)$ can be expressed as follows [30]:

$$C_L(t)=\underbrace{f\left[q(t)+\varphi(L_c)\frac{\dot{\eta}(t)}{U}\right]}_{\text{VIV force coefficient}}-\underbrace{\sum_{i=1}^{n}A_i\left[\varphi(L_c)\frac{\dot{\eta}(t)}{U}\right]^i}_{\text{Galloping force coefficient}} \tag{4}$$

$C_L(t)$ consists of two parts: the VIV force component and the galloping force component, which are interconnected by the VIV-galloping coupled coefficient f. A_i is the galloping force coefficient, where $i=1, 3$. In this study, the aerodynamic force is approximated by a third-order polynomial, as higher order nonlinear terms have been widely investigated in previous works and found to have minimal impact on the galloping amplitude for bluff bodies with symmetric aerodynamic characteristics [31]. A_i can be determined using the least square method based on the aerodynamic parameters obtained from computational fluid dynamics (CFD) simulations at different attack angles [32]. It should be noted that C_D is included in A_1. $q(t)$ is related to the VIV behavior and describes the near-wake vortex motion, which is governed by the Van der Pol wake oscillator equation [33]

$$\ddot{q}(t)-2\lambda\omega_V\left[1-\left(\frac{2f}{C_{L0}}q(t)\right)^2\right]\dot{q}(t)+\omega_V^2 q(t)$$
$$=-\varphi(L_c)\omega_V^2\frac{\dot{\eta}(t)}{U}-\varphi(L_c)\gamma\ddot{\eta}(t) \tag{5}$$

$$\lambda=\frac{Df}{2\sqrt{2}\pi^2 H} \tag{6}$$

where λ is the damping ratio of the wake oscillator, $\omega_V=2\pi USt/D$ is the vortex shedding frequency, C_{L0} is the amplitude of the lift force coefficient, St is the Strouhal number, and γ is a constant related to the aspect ratio of the bluff body.

Assuming the external load of the VGPEH is a simple resistor R_L, according to Kirchhoff's current law [34]

$$\Theta\dot{\eta}(t)=\frac{V(t)}{R_L}+C_p\dot{V}(t) \tag{7}$$

where C_p is the clamped capacitance of the piezoelectric transducer of the VGPEH.

By the equivalent lumped parameter representation $M_{eff}=1/\varphi^2(L_c)$, $C_{eff}=2\omega_n\zeta/\varphi^2(L_c)$, $K_{eff}=\omega_n^2/\varphi^2(L_c)$, $\theta=\Theta/\varphi(L_c)$, $z(t)=\varphi(L_c)\eta(t)$, the SDOF lumped parameter model of the VGPEH is shown in Fig. 2(b) and the governing equations can be written as follows:

$$M_{eff}\ddot{z}(t)+C_{eff}\dot{z}(t)+K_{eff}z(t)+\theta V(t)=$$
$$-\frac{1}{2}\rho U^2 DH\left[f\left(q(t)+\frac{\dot{z}(t)}{U}\right)-\sum_{i=1}^{n}A_i\left(\frac{\dot{z}(t)}{U}\right)^i\right] \tag{8}$$

$$\ddot{q}(t)-2\lambda\omega_V\left[1-\left(\frac{2f}{C_{L0}}q(t)\right)^2\right]\dot{q}(t)+\omega_V^2 q(t)$$
$$=-\omega_V^2\frac{\dot{z}(t)}{U}-\gamma\ddot{z}(t) \tag{9}$$

$$\theta\dot{z}(t)=\frac{V(t)}{R_L}+C_p\dot{V}(t) \tag{10}$$

where M_{eff} is the equivalent mass, C_{eff} is the equivalent damping, K_{eff} is the equivalent stiffness, and θ is the electro-mechanical coupling coefficient, and $z(t)$ is the displacement of the bluff body. Similar to VIV and galloping, we can conclude that VIV-galloping coupled vibration is also a type of self-excited oscillation caused by the uneven pressure distribution on the upper and lower surfaces of a bluff body [35], [36].

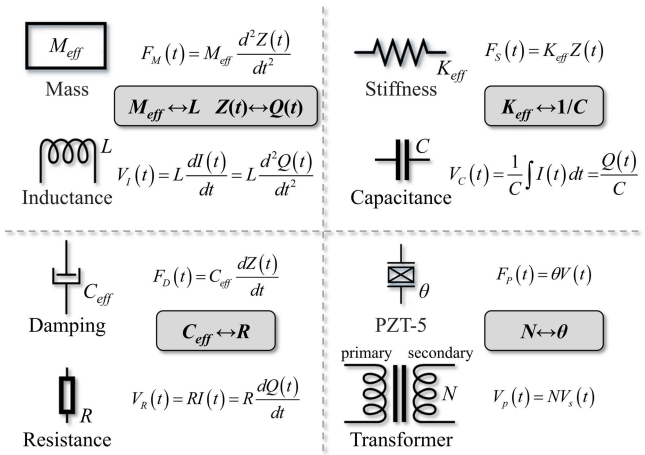

Fig. 3. Equations and analogies between mechanical and electrical quantities.

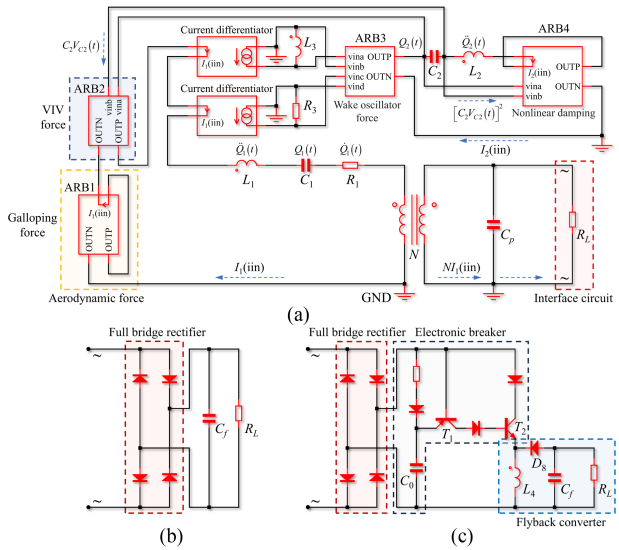

Fig. 4. (a) Equivalent circuit model of the VGPEH connected to a simple resistive load. (b) Standard energy harvesting (SEH) circuit. (c) Self-powered synchronous electric charge extraction (SP-SECE) circuit.

B. Equivalent Circuit Model

To facilitate the coupling of the multiphysics fields—fluid, mechanical, and particularly electrical—an equivalent circuit model for the VGPEH is developed, leveraging the electro-mechanical analogous relationship compared and outlined in Fig. 3.

According to Fig. 3, (7)–(9) can be transformed into inductance-resistance-capacitance resonance circuit representation using the electro-mechanical analogy:

$$L_1\ddot{Q}_1(t)+R_1\dot{Q}_1(t)+C_1Q_1(t)+NV(t)$$
$$=-\frac{1}{2}\rho U^2DH\left[f\left(Q_2(t)+\frac{\dot{Q}_1(t)}{U}\right)-\sum_{i=1}^{n}A_i\left(\frac{\dot{Q}_1(t)}{U}\right)^i\right] \tag{11}$$

$$L_2\ddot{Q}_2(t)-2\beta\omega_V\left[1-\left(\frac{2f}{C_{L0}}Q_2(t)\right)^2\right]\dot{Q}_2(t)+C_2Q_2(t)$$
$$=-\omega_V^2\frac{\dot{Q}_1(t)}{U}-\gamma\ddot{Q}_1(t) \tag{12}$$

$$N\dot{Q}_1(t)=\frac{V(t)}{R_L}+C_p\dot{V}(t) \tag{13}$$

where N is turns ratio of the transformer, using Ohm's law $V(t)=R\times\dot{Q}(t)$ and $V(t)=L\times\ddot{Q}(t)$, $\dot{Q}_1(t)$ and $\ddot{Q}_1(t)$ in (11) can be derived. As shown in Fig. 4(a), the ECM for the VGPEH connected to a simple resistive load can be built according to (10)–(12). With the multiphysics fields translated into electrical terms and represented within the circuit simulation software SIMetrix, the resistive load can be replaced with any other interface circuits, such as the standard energy harvesting (SEH) circuit, as shown Fig. 4(b), and self-powered synchronous electric charge extraction (SP-SECE) circuit shown in Fig. 4(c). The SEH circuit comprises a full bridge rectifier and a filter capacitor C_f. The SP-SECE circuit comprises a full bridge rectifier, an electronic breaker, and a flyback converter. T_1 and T_2 conduct only at the instant when the voltage reaches the maximum. During this short instant, the charge accumulated in the piezoelectric transducer quickly transfers to inductor L_4 in the flyback converter and is thereby transferred to filter capacitor C_f. Finally, the energy dissipates on the external load resistance R_L through diode D_8. Moreover, $C_0=4.7$ nF is chosen to ensure that the SP-SECE circuit can successfully operate in both experiment and circuit simulation.

The four blocks, i.e., ARB1, ARB2, ARB3, and ARB4 in Fig. 4(a), are user-defined arbitrary sources that respectively denote the VIV force, the galloping force, the wake oscillator force, and the nonlinear resistive term in (10) and (11). Specifically, the four arbitrary voltage sources are defined as follows:

$$\begin{cases}\text{ARB1}=-\frac{1}{2}\rho U^2DH\left\{f\left[C_2V_{C2}+\frac{I_1(\text{iin})}{U}\right]\right\}\\ \text{ARB2}=\frac{1}{2}\rho U^2DH\sum_{i=1}^{n}A_i\left[\frac{I_1(\text{iin})}{U}\right]^i\\ \text{ARB3}=-\frac{\omega_V^2}{U}\frac{V_{R3}}{R_3}-\gamma\frac{V_{L3}}{L_3}\\ \text{ARB4}=2\beta\omega_V\left(1-\frac{4f^2}{C_{L0}^2}C_2^2V_{C2}^2\right)I_2(\text{iin})\end{cases} \tag{14}$$

The "current differentiator" module functions, as its name suggests, as a differentiator to output current proportional to the input current I(iin), which corresponds to the first derivative of the charge, i.e., $\dot{Q}(t)$, as appeared on the right-hand side of (11). In ARB1 and ARB2, $I_1(\text{iin})=\dot{Q}_1(t)$; while in ARB4, $I_2(\text{iin})=\dot{Q}_2(t)$.

IV. Experimental Setup

The prototyped VGPEHs used in the study are shown in Fig. 5(a). Detailed material properties and geometric dimensions of the structures are listed in Table I. The prototyped VGPEHs are fixed on a vertical frame and implemented on a baseplate. The whole experimental apparatus is tested in a low turbulence circulation wind tunnel, as shown in Fig. 5(b) and (c). The ac output voltage generated by the VGPEH can be regulated by different interface circuits on the circuit board shown in Fig. 5(d)

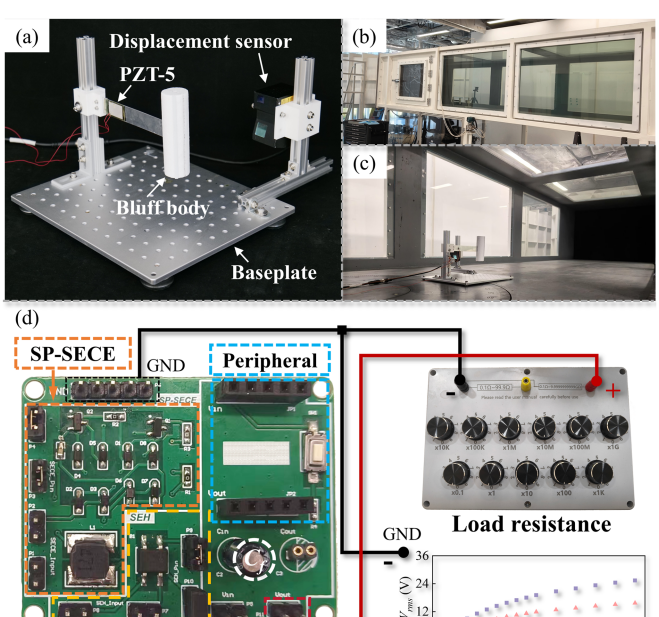

Fig. 5. Brief overview of the experiment setup. (a) Prototyped VGPEH. (b) Test section of the wind tunnel. (c) Implementation of the VGPEH in the wind tunnel. (d) Printed circuit board for the interface circuits, including the SP-SECE circuit and the SEH circuit.

TABLE I
MATERIAL PROPERTIES AND GEOMETRIC PARAMETERS OF THE VGPEH

System Parameter	Material Property	Size	
		Length × Width × Height (mm)	Diameter × Height (mm)
Bluff body	Expandable polystyrene	\	35 × 120
Cantilever beam	1060 pure aluminum	200 × 25 × 0.6	\
Piezoelectric sheet	PZT-5	30 × 20 × 0.4	\
Frame	Aluminum alloy	20 × 20 × 200	\
Fixture	Polylactic acid	\	\
Baseplate	Stainless steel	320 × 280 × 8	\

and the regulated output voltage can be adjusted by changing the load resistance.

The output voltage produced by the VGPEH is measured by a dual-channel digital oscilloscope (Analog Discovery 2), and the displacement of the bluff body is captured using a laser displacement sensor (SG6150). The wind speed U is gauged by a pitot tube and controlled by adjusting the frequency f of the drought fan. The relationship between U and f follows $U = 0.87f - 0.038$.

V. RESULTS AND DISCUSSIONS

A. Experimental Results

Fig. 6 shows the root mean square (RMS) open circuit (OC) voltage outputs and displacement responses of the six VGPEH prototypes obtained from the experimental tests as a function of the wind speed U. The results of two baseline models, i.e.,

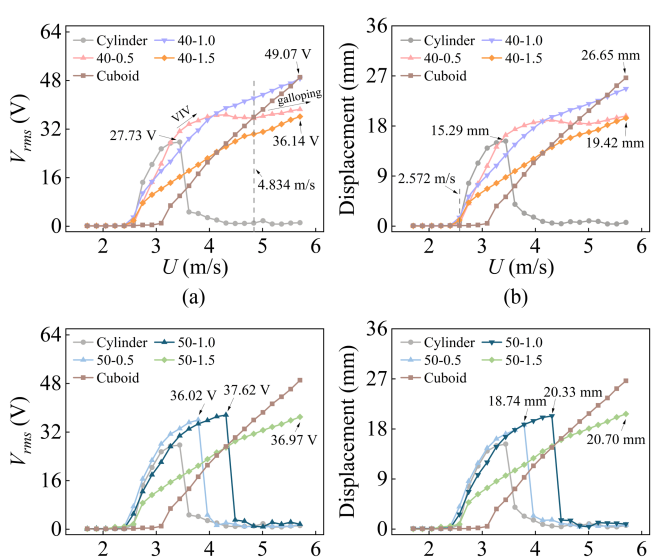

Fig. 6. Experimentally obtained results. (a)&(c) RMS open circuit (OC) voltage outputs of the six VGPEHs versus the wind speed U. (b)&(d) Displacement responses of the six VGPEHs versus the wind speed U.

PEHs with cylinder and cuboid bluff bodies, are also presented for comparison. The PEH with a cylinder bluff body, which is a typical VIVPEH, exhibits characteristic VIV responses with an operational bandwidth (lock-in region) of 2.572–3.616 m/s, a maximum RMS OC voltage of 27.73 V, and a maximum displacement of 15.29 mm. In contrast, the other baseline model, featuring a cuboid bluff body and representing a typical GPEH, demonstrates characteristic galloping behavior, with dynamic responses increasing monotonically with wind speed, reaching a maximum RMS OC voltage of 49.07 V and a maximum displacement of 26.65 mm at the maximum wind speed 5.704 m/s tested in the wind tunnel experiment. For brevity, the term 'xx bluff body' will be used hereinafter to refer to the PEH with the corresponding bluff body, except for the typical VIVPEH and GPEH used as baseline models.

On one hand, compared to the VIVPEH, the responses, i.e., voltage and displacement, of the three VGPEHs shown in Fig. 6(a) and (b), with $\alpha_1 = 40°$, are not constrained by the lock-in region and are significantly enhanced at higher wind speeds. In other words, by attaching strips to the bluff body at an angle of 40°, the behavior of the VGPEH transitions prominently into galloping. On the other hand, compared to the GPEH, the onset wind speeds of the three VGPEHs are reduced to levels similar to that of the VIVPEH. Therefore, the three VGPEHs shown in Fig. 6(a) and (b) combine the advantages of both VIVPEH and GPEH. The 40–1.0 and 40–1.5 bluff bodies demonstrate classic galloping characteristics. The maximum RMS OC voltage outputs attained by the two VGPEHs are 48.68 and 36.14 V, respectively, with the corresponding maximum displacements of 26.65 and 19.42 mm, respectively. Their onset wind speeds are basically maintained at 2.572 m/s. Notably, the 40–0.5 bluff body exhibits distinct VIV-galloping coupled vibration characteristics. Vortex-induced vibration is observed

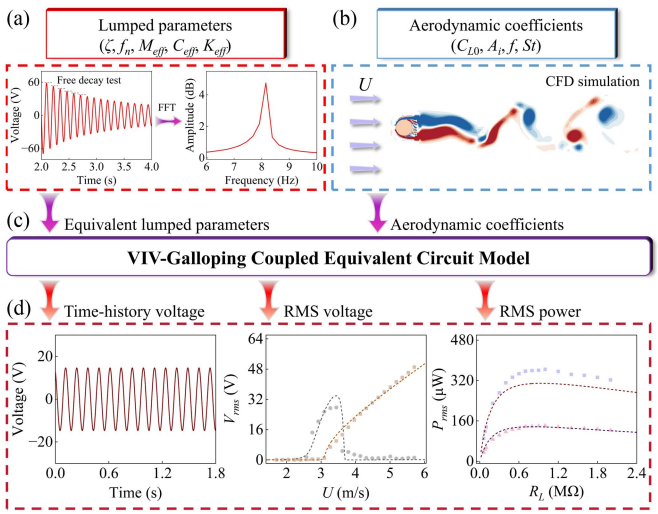

Fig. 7. Flowchart of the ECM simulation procedures.

within the wind speed range of 2.572–4.834 m/s, transitioning into the galloping region beyond $U = 4.834$ m/s. A hump between the two regions signifies this transition. The maximum RMS OC voltage and displacement obtained are 38.50 V and 19.80 mm, respectively. Compared with the VIVPEH, the maximum RMS OC voltage of the 40–0.5 bluff body increased by 38.84%, and the maximum displacement increased by 29.50%.

Unlike the three VGPEHs shown in Fig. 6(a) and (b), the other three counterparts, shown in Fig. 6(c) and (d), with $\alpha_1 = 50°$ are not consistent and exhibit different behaviors. The 50–0.5 and 50–1.0 bluff bodies display VIV characteristics but with broadened working bandwidths of 2.572–3.964 and 2.572–4.486 m/s, respectively. The maximum RMS OC voltage outputs of the two VGPEHs are 36.02 and 37.62 V, respectively, with the corresponding maximum displacements of 18.74 and 20.33 mm. In contrast, similar to the cases in Fig. 6(a) and (b), the 50–1.5 bluff body demonstrates clear galloping characteristics, with an onset wind speed of 2.572 m/s, achieving a maximum RMS OC voltage of 36.97 V and a maximum displacement of 20.70 mm at 5.704 m/s.

B. ECM Simulation

The procedures for performing the ECM simulation are illustrated in Fig. 7. According to Fig. 7(a), the damping ratio of the VGPEH ζ can be determined via the free decay test, and the natural frequency f_n can be identified by the fast Fourier transform. The equivalent lumped parameters of the VGPEH are identified and summarized in Table II following the experimental identification [37], [38]. A load resistance $R_L = 100$ MΩ is used to simulate the open circuit condition.

As shown in Fig. 7(b), the CFD simulation is conducted to determine the aerodynamic force coefficients of the bluff bodies. The incoming flow U is set as $U = 3.2$ m/s, and the Reynolds number is determined to be 7600, indicating a turbulent state in the wake region. The wall-adapting local eddy viscosity model is employed in the simulation for its good properties in laminar and turbulent flows, as well as its adaptability for near-wall and

TABLE II
EQUIVALENT LUMPED PARAMETERS OF THE VGPEH

System Parameter	Value	Unit
M_{eff}	10.28	g
ζ	1.02×10^{-2}	/
C_{eff}	1.08×10^{-2}	N·s/m
K_{eff}	27.09	N/m
f_n	8.17	Hz
C_p	32.45	nF
θ	2.02×10^{-4}	N/V
γ	0.255	/

TABLE III
AERODYNAMIC COEFFICIENTS OF DIFFERENT BLUFF BODIES IDENTIFIED FROM CFD SIMULATION

	A_1	A_3	f	C_{L0}	St
Cylinder	\	\	0.82	0.078	0.105
Cuboid	1.37	-86.4	0	1.353	\
40-0.5	0.75	-105.5	1.41	0.108	0.100
40-1.0	1.65	-100.17	0	0.369	\
50-0.5	\	\	1.60	0.147	0.106

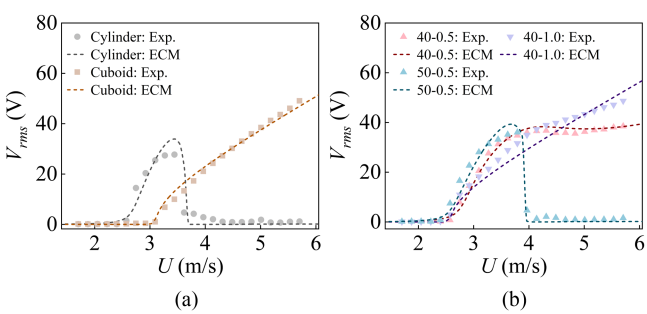

Fig. 8. Comparison of the experimental and ECM simulation results of the RMS OC voltage of the WIVPEHs: (a) Two baseline models. (b) Three VGPEH models (Exp. represents the experimental results).

far-field analyses [39]. The aerodynamic force coefficients of different bluff bodies identified in the CFD simulation are listed in Table III.

Three bluff body configurations and two control models were selected to evaluate the ECM's ability to simulate distinct flow-induced vibration mechanisms. The cylinder and cuboid bluff bodies serve as control cases. The 40–0.5 bluff body, exhibiting VIV-galloping coupling, represents a key focus of this study. One additional bluff body was chosen for its dominant VIV response, and another for its galloping behavior, enabling validation of the ECM across different vibration types.

The identified lumped parameters and the aerodynamic coefficients can be substituted into the equivalent circuit model shown in Fig. 7(c), and various responses of VGPEH, like time-history voltage, RMS voltage, and RMS power shown in Fig. 7(d), can be studied and analyzed via ECM simulations. Fig. 8 shows the ECM simulation results for several representative models and compares them with the experimental results. The results for the two baseline models are displayed in Fig. 8(a). To ensure clarity and avoid redundancy, the results for three VGPEHs are plotted separately in Fig. 8(b). Although some discrepancies exist between the experimental and simulation results, it can be found that the ECM simulation model can effectively capture

and distinguish the overall characteristics of different models well. In particular, the hump on the curve of the 40-0.5 bluff body that indicates the VIV-galloping coupled effect can also be well identified in the simulation.

In the following, we offer some discussions and explanations of the aerodynamics and simulation results of the WIVPEHs shown in Table III and Fig. 8. From the information given in Table III, it is easy to infer that the cuboid and 40–1.0 bluff bodies should only exhibit galloping characteristics because $f = 0$, which causes the VIV-related aerodynamic terms in (3) to be zero and decouples (8) from (7), resulting in the disappearance of VIV characteristics, as shown in Fig. 8. According to the onset wind speed formula for GPEHs, i.e., $U_c = 2C_{eff}/(\rho DHA_1)$, the onset wind speed U_c decreases as A_1 increases. As shown in Table III, the 40–1.0 bluff body has a larger A_1 value of 1.65 compared to 1.37 for the cuboid bluff body. Thus, the 40–1.0 bluff body, with its higher A_1, becomes unstable and initiates vibration at a lower wind speed than the GPEH with the cuboid bluff body. Furthermore, the cylinder and 50–0.5 bluff bodies predominantly manifest VIV phenomena because their galloping force coefficients identified from the CFD simulation are equal to zero, i.e., $A_i = 0$ in Table III. As (3) indicates, a larger f implies a stronger VIV force, and a larger C_{L0} in (4) reduces the damping effect of wake oscillation. Given the data in Table III, it becomes evident why the 50–0.5 bluff body has a wider operational bandwidth and generates higher voltage outputs. Notably, for the 40–0.5 bluff body, its $f = 1.41$ is larger than that of the cylinder bluff body, and its $A_1 = 0.65$ is smaller than that of the cuboid bluff body. This explains why it generates higher voltage outputs in the VIV region at low wind speeds and transitions to galloping characteristics at high wind speeds to maintain a high voltage output.

C. Output Performance With Different Circuits

Building on the ECM simulation model validated in the previous section, this section examines the influences of connecting the VGPEH to various interface circuits. Given that the VGPEH with the 40–0.5 bluff body exhibits distinct VIV-galloping coupled vibrations, it is selected for use in the following study. For simplicity, the term "VGPEH" will hereafter refer to the one with the 40–0.5 bluff body unless otherwise specified. The RMS power P_{rms} in this section is defined as $P_{rms} = V_{rms}^2/R_L$.

1) AC Circuit: In most studies on flow-induced vibration energy harvesting, only a resistive load R_L is considered for the sake of simplicity. Since the response of a WIVPEH is an alternating current (ac), such a circuit is referred to as an ac circuit. Fig. 9 presents the output performance of the VGPEH connected to an ac circuit. The experimental results shown in Fig. 9(a) indicate that the RMS voltage, V_{rms}, produced by the VGPEH increases as the load resistance R_L increases at $U = 3.094$ m/s and $U = 3.442$ m/s, while the RMS power P_{rms} in Fig. 9(b) first increases and then decreases. At the optimal load resistance R_{opt} of about 0.6 MΩ, a maximum P_{rms} of 180.95 μW is generated at $U = 3.094$ m/s and 497.36 μW at $U = 3.442$ m/s. The simulated RMS voltage and power versus the load resistance are also plotted in Fig. 9(a) and (b). Relatively good agreement is

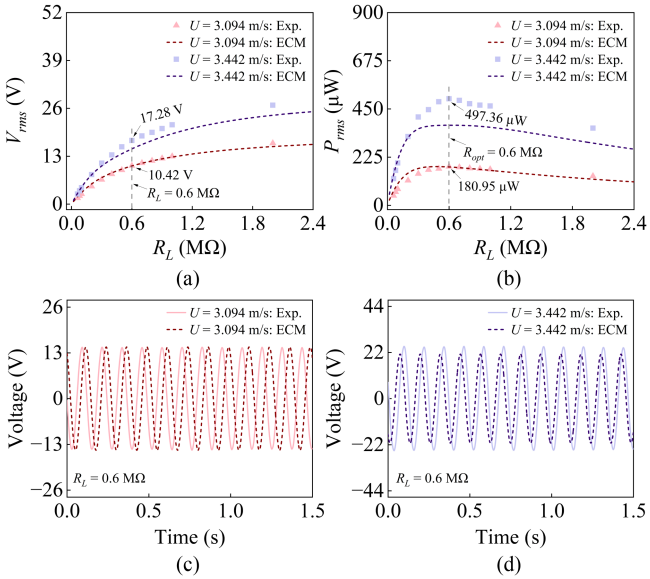

Fig. 9. Experimentally measured and ECM simulated outputs of the VGPEH with the 40–0.5 bluff body connected to an ac circuit. (a) RMS voltage outputs V_{rms} versus the load resistance. (b) RMS output power outputs P_{rms} versus the load resistance. (c) Steady-state time-history voltage responses at $R_L = 0.6$ MΩ and $U = 3.094$ m/s. (d) Steady-state time-history voltage response at $R_L = 0.6$ MΩ and $U = 3.442$ m/s.

observed between the experimentally measured results and simulation predictions across the range of load resistance examined. The voltage discrepancy is relatively small, but the difference in the RMS power output is more pronounced due to the squaring of the voltage value, making the RMS power discrepancy appear more significant. Under the ac circuit condition, the averaged power discrepancy between the experiment and circuit simulation is 13.83% at $U = 3.094$ m/s and 15.73% at $U = 3.442$ m/s across the range of $R_L = 0.02$–2.0 MΩ. Furthermore, Fig. 9(c) and (d) plot and compare the time-history responses measured and simulated. The experiment results are higher than that of the simulated ones at $U = 3.094$ m/s and $U = 3.442$ m/s. As shown in Fig. 8(b), a similar discrepancy between experimental and ECM simulation is noted. This may be attributed to errors in the parameter identification process, including lumped and aerodynamic parameters [40], [41]. However, given the complexity of the multiphysics interaction problem, such discrepancies are challenging to avoid.

2) DC Circuit: The direct output from a WIVPEH is ac, whereas most low-power electronic devices require a dc power supply. Thus, a rectifier bridge is needed to realize ac-to-dc conversion. Such a rectifier bridge circuit is often referred to as a dc circuit or a SEH circuit. In a similar way, experiments and circuit simulations were conducted to evaluate the DC circuit. The results are presented in Fig. 10. The optimal load resistance R_{opt} is experimentally determined to be about 1.0 MΩ in Fig. 10(b), at which a maximum P_{rms} of 140.92 μW is achieved under $U = 3.094$ m/s and 364.17 μW under $U = 3.442$ m/s. Compared to the ac circuit, the maximum power harvested by the dc circuit at two wind speeds are over 20% lower than that of the ac circuit. This reduction may be attributed to the voltage

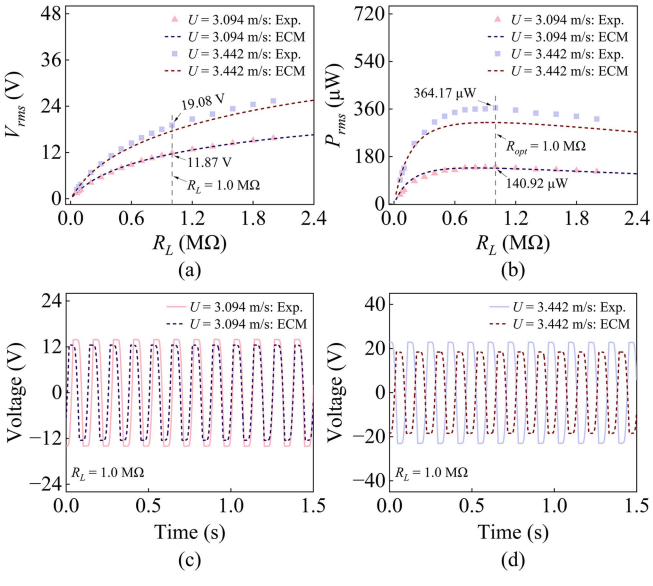

Fig. 10. Experimentally measured and ECM simulated outputs of the VGPEH with the 40–0.5 bluff body connected to a dc circuit. (a) RMS voltage outputs V_{rms} versus the load resistance. (b) RMS output power outputs P_{rms} versus the load resistance. (c) Steady-state time-history voltage responses at $R_L = 1.0$ MΩ and $U = 3.094$ m/s. (d) Steady-state time-history voltage response at $R_L = 1.0$ MΩ and $U = 3.442$ m/s.

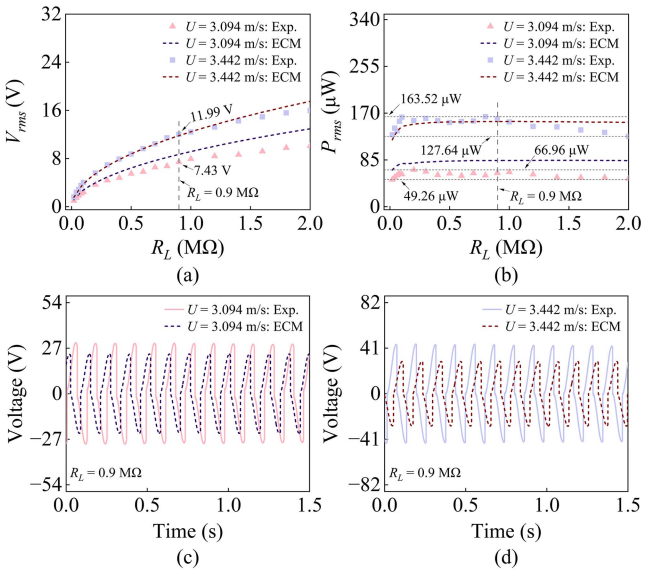

Fig. 11. Experimentally measured and ECM simulated outputs of the VGPEH with the 40–0.5 bluff body connected to a SP-SECE circuit. (a) RMS voltage outputs V_{rms} versus the load resistance. (b) RMS output power outputs P_{rms} versus the load resistance. (c) Steady-state time-history voltage responses at $R_L = 0.9$ MΩ and $U = 3.094$ m/s. (d) Steady-state time-history voltage response at $R_L = 0.9$ MΩ and $U = 3.442$ m/s.

drop of the rectifier bridge. The simulated V_{rms} and P_{rms} under $U = 3.094$ m/s and $U = 3.442$ m/s are also plotted in Fig. 10(a) and (b), demonstrating good agreement with the experimental results. Under the dc circuit condition, the averaged power discrepancy between the experiment and circuit simulation is 7.94% at $U = 3.094$ m/s and 9.74% at $U = 3.442$ m/s across the range of $R_L = 0.02$–2.0 MΩ. Additionally, the time-history voltage responses of the VGPEH are depicted in Fig. 10(c) and (d), where strong correlations are observed in terms of both voltage amplitudes and waveforms.

3) SP-SECE Circuit: To further demonstrate the value and highlight the utility of the ECM simulation model, a self-powered synchronous electric charge extraction (SP-SECE) circuit is shunted to the VGPEH in the study. Corresponding experiments and simulations are also carried out. Like the voltage behavior in other circuits, Fig. 11(a) shows that the RMS voltage V_{rms} also increases with the increase of R_L at $U = 3.094$ m/s and $U = 3.442$ m/s. Regarding the power as depicted by the experimental results in Fig. 11(b), the maximum power harvested by the SP-SECE circuit is 66.96 μW at $U = 3.904$ m/s. Similarly, at $U = 3.442$ m/s, the SP-SECE circuit harvests a maximum power of 163.52 μW. Although the power output of the VGPEH decreases by over 50% when using the SP-SECE circuit, Fig. 11(b) shows that it delivers a relatively stable power output across the range of $R_L = 0.02$–2.0 MΩ: P_{rms} fluctuates within [49.26, 66.96] μW at $U = 3.094$ m/s, and [127.64, 163.52] μW at $U = 3.442$ m/s. As shown in Fig. 11(b), simulation results also show significantly greater stability and are quite consistent with the experimental results. Under the SP-SECE circuit condition, the averaged power discrepancy between the experiment and circuit simulation is 33.47% at $U = 3.094$ m/s and 9.82% at $U = 3.442$ m/s across the range of $R_L = 0.02$–2.0 MΩ. Since the SP-SECE circuit in the simulation is more ideal and exhibits lower dissipation, the simulated power output is more stable compared to the experimental results. This power stability is attributed to the load-independent nature of the SECE circuit [42]. The time-history voltage responses of the VGPEH connected to an SP-SECE circuit are illustrated in Fig. 11(c) and (d). Both experimental and simulation waveforms indicate that the SP-SECE functions well as the voltage periodically flips to zero at the peaks. Unfortunately, the discrepancy between the two results becomes noticeable under the SP-SECE condition, likely due to a combination of multiple factors, including errors in the system parameter identification and inaccuracies in modeling the nonlinear components of the SP-SECE circuit [43]. Moreover, parasitic resistance, forward voltage drops of diodes and transistors, and nonideal switching characteristics—such as finite switching times and delays—can adversely affect the timing and efficiency of the SP-SECE circuit. These real-world imperfections, not fully captured in the idealized model, contribute to the observed discrepancies in energy harvesting performance under weak coupling [44], [45].

A detailed P_{rms} of experimental results comparison between the dc and SP-SECE circuits is summarized in Table IV. P_{opt} is the optimal P_{rms}, P_{min} is the minimum P_{rms}, ΔP_{rms} is the power fluctuation, defined as: $\Delta P_{rms} = P_{opt} - P_{min}$. One can find in Table IV that ΔP_{rms} of the SP-SECE circuit is smaller than that of the dc circuit, and P_{opt} of the dc circuit is higher than that of the SP-SECE circuit, indicating that the SP-SECE circuit delivers a lower but more stable power output than the dc circuit.

The above results from both experiments and simulations indicate that the SP-SECE circuit outperforms traditional ac

TABLE IV
EXPERIMENTAL RESULTS COMPARISON OF P_{OPT}, P_{MIN}, ΔP_{RMS} BETWEEN DC CIRCUIT AND SP-SECE CIRCUIT

	$U = 3.094$ m/s		$U = 3.442$ m/s	
	DC	SP-SECE	DC	SP-SECE
P_{opt} (μW)	140.92	66.96	364.17	163.52
P_{min} (μW)	35.46	49.26	90.88	127.64
R_{opt} (MΩ)	1.0	/	1.0	/
ΔP_{rms} (μW)	105.46	17.70	273.29	35.88

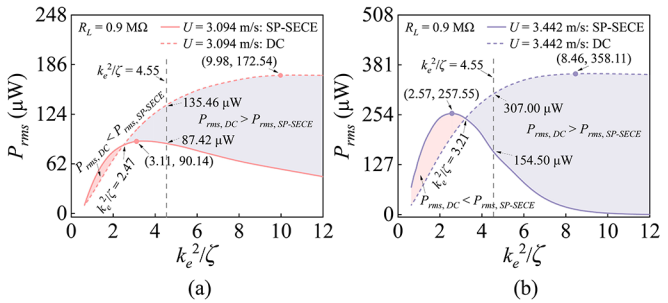

Fig. 12. Variation of the RMS power output P_{rms} at $R_L = 0.9$ MΩ versus k_e^2/ζ for the SP-SECE and dc circuits at (a) $U = 3.094$ m/s and (b) $U = 3.442$ m/s.

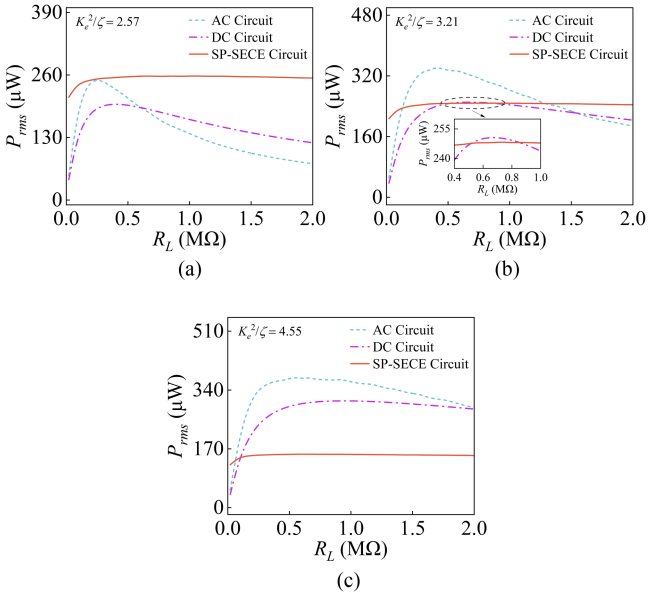

Fig. 13. Variation of the RMS power output at $U = 3.442$ m/s versus the load resistance for ac, dc, and SP-SECE circuits under different coupling conditions. (a) Weak coupling condition with $K_e^2/\zeta = 2.57$. (b) Medium coupling condition with $K_e^2/\zeta = 3.21$. (c) Strong coupling condition with $K_e^2/\zeta = 4.55$.

and dc circuits in terms of power stability but delivers lower power magnitude. This seems to contradict those conclusions by previous studies, which suggested that the SP-SECE circuit should excel in both power stability and power magnitude [46]. In fact, the above conclusion is not universally applicable. The SP-SECE circuit can only enhance the performance and efficiency of energy harvesters operating under weak coupling conditions. To support this statement, we first introduce a dimensionless electro-mechanical coupling coefficient k_e, which can be calculated by the formula $k_e^2 = \theta^2/C_p K_{eff}$ [47]. Based on the ECM model, we varied the clamped capacitance of the piezoelectric transducer C_p to increase the coupling strength k_e to examine the consequences.

As shown in Fig. 12, the power output of the SP-SECE circuit first increases with k_e^2 and reaches the maximum value, then decreases with k_e^2. The maximum output power for SP-SECE circuits is 90.14 μW at $k_e^2 = 3.11$ when $U = 3.094$ m/s and 257.55 μW at $k_e^2 = 2.57$ when $U = 3.442$ m/s, respectively. The power output of the dc circuit continuously grows with k_e^2/ζ and then tends to saturate. The maximum output power for dc circuits reaches 172.54 μW when $k_e^2 = 9.98$ at $U = 3.094$ m/s and 358.11 μW when $k_e^2 = 8.46$ at $U = 3.442$ m/s, respectively. This power saturation phenomenon is consistent with the power limit theory in studies [48] and [49]. It is important to note in Fig. 12 that the power output of the SP-SECE circuit is larger than that of the dc circuit when $k_e^2 < 2.47$ at $U = 3.094$ m/s and $k_e^2 < 3.21$ at $U = 3.442$ m/s. The above result can be easily understood and remembered as follows: the SP-SECE circuit outperforms the dc circuit under weak coupling conditions but underperforms under strong coupling conditions. According to Table II, the value of k_e^2/ζ of our VGPEH is calculated to be 4.55. Using the region division shown in Fig. 12, it explains why the $P_{rms,DC}$ is larger than $P_{rms,SP\text{-}SECE}$ at both $U = 3.094$ m/s and $U = 3.442$ m/s. Moreover, from Fig. 12, we can quickly find that $P_{rms,SP\text{-}SECE} = 87.42$ μW and $P_{rms,DC} = 135.46$ μW at $k_e^2 = 4.55$ when $U = 3.094$ m/s. Similarly, $P_{rms,SP\text{-}SECE} = 154.50$ μW and $P_{rms,DC} = 307.00$ μW at the same k_e^2/ζ when $U = 3.442$ m/s. These results are consistent with the simulation results presented in Fig. 11(b).

Moreover, to more clearly compare the variation of P_{rms} among the three interface circuits under different coupling conditions, Fig. 13 shows the P_{rms} values for the ac, dc, and SP-SECE circuits at three selected values of normalized electromechanical coupling, $K_e^2/\zeta = 2.57$, $K_e^2/\zeta = 3.21$, and $K_e^2/\zeta = 4.55$, representing weak, medium, and strong coupling conditions. As shown, the RMS power output of the ac and dc circuits increases progressively with higher K_e^2/ζ, while the SP-SECE circuit exhibits a decreasing trend in P_{rms} as the coupling strength (K_e^2/ζ) increases. These observations are consistent with the simulation results shown in Fig. 12(b) for $K_e^2/\zeta > 2.57$. Based on Fig. 13, a detailed comparison of the simulation results (P_{opt}, P_{rms}, and ΔP_{rms}) under different coupling conditions is summarized in Table V. From both Fig. 13 and Table V, it can be observed that the SP-SECE circuit delivers the maximum power output across varying load resistances under weak coupling conditions. Furthermore, the SP-SECE circuit demonstrates more stable power performance across different coupling regimes compared to the ac and dc circuits.

Given these findings, it becomes evident that the performance of the SP-SECE circuit remains to be improved under strong coupling conditions. A promising approach is to enhance the power output of VGPEHs under strong coupling conditions by optimizing the SP-SECE circuit, such as through the use of a

TABLE V
COMPARISON OF P_{OPT}, P_{MIN}, ΔP_{RMS} AT $U = 3.442$ *m/s* AMONG AC, DC, AND SP-SECE CIRCUIT UNDER DIFFERENT COUPLING CONDITIONS

K_e^2/ζ		P_{opt} (μW)	P_{min} (μW)	ΔP_{rms} (μW)
$K_e^2/\zeta = 2.57$ (Weak coupling)	AC	249.66	50.98	198.68
	DC	199.48	42.19	157.29
	SP-SECE	258.03	213.75	44.28
$K_e^2/\zeta = 3.21$ (Medium coupling)	AC	343.11	51.19	291.92
	DC	250.70	37.25	213.45
	SP-SECE	248.35	207.38	40.97
$K_e^2/\zeta = 4.55$ (Strong coupling)	AC	377.11	51.35	325.76
	DC	308.77	38.23	270.54
	SP-SECE	154.67	123.94	30.73

TABLE VI
PERFORMANCE COMPARISONS BETWEEN THE REFERRED AND PROPOSED HARVESTERS

Reference	Wind speed (m/s)	Output power (μW)	Power density (μW/cm^3)
Wang et al. [51]	3.6	187	1.59
Sun et al. [52]	6.0	56.49	0.35
Hu et al. [53]	6.0	72	0.16
Poudel et al. [54]	4.0	108	1.08
This work	3.442	497.36	4.23

tunable SP-SECE circuit [50] and a hybrid SP-SSHI and SECE circuit [14].

In the final section, we present a detailed comparison of the performance between several referenced and our proposed wind energy harvesters, as shown in Table VI. The power density is defined as P_{out}/V_m, where P_{out} is the power output, and V_m is the volume of the harvester. The proposed harvester achieves a power density of 4.23 μW/cm^3 at a wind speed of 3.442 m/s, demonstrating superior output performance at relatively low wind speeds compared to the other designs.

VI. CONCLUSION

This work has proposed a comprehensive ECM for the modeling and analysis of VGPEHs. Surface strips were introduced to the cylinder bluff body of a traditional VIVPEH to induce VIV-galloping coupled vibrations. The influences of the strip height (h_1) and installation angle (α_1) were investigated. The results indicated that an optimal strip configuration could transition the vortex-induced vibration of the bluff body into galloping. A bluff body with a strip installation angle $\alpha_1 = 40°$ and strip height $h_1 = 0.5$ mm demonstrated a distinct VIV-galloping coupled effect among multiple designs in the wind tunnel experiment. Compared with a baseline VIVPEH, the maximum RMS open-circuit voltage of the VGPEH featuring the VIV-galloping coupled effect increased by 38.84% while the cut-in wind speed remained unchanged.

The governing equations of the VGPEH with the VIV-galloping coupled effect were derived, the aerodynamic coefficients were determined through CFD simulations, and an equivalent circuit model was developed leveraging electro-mechanical analogies. The equivalent circuit model was validated via wind tunnel experiments. The results showed that the ECM can effectively capture and distinguish the overall characteristics of different models well. Furthermore, the ECM was utilized to incorporate advanced interface circuits into the analysis. The simulation results were compared with the experimental counterparts for validation. According to the experimental results, the optimal load resistance R_{opt} for the ac circuit is 0.6 MΩ, and for the dc circuit, it is 1.0 MΩ. The two circuits achieve their maximum power outputs at the corresponding optimal resistances. For the SP-SECE circuit, the output power is theoretically independent of the load resistance. Both the experimental observation and simulation prediction confirmed this feature: $P_{rms,\,SP\text{-}SECE}$ varied slightly in the range of $R_L = 0.02$–2 MΩ. However, unlike the conclusions in the previous studies, compared with the dc circuit, $P_{rms,\,SP\text{-}SECE}$ is reduced by about 55.10% when $U = 3.442$ m/s. To resolve this contradiction, we introduced a dimensionless electro-mechanical coupling coefficient. Through an analysis based on the equivalent circuit model, we demonstrated that the SP-SECE circuit outperforms the dc circuit only under weak coupling conditions, whereas the prototyped VGPEH operates as a strongly coupled system.

The developed VGPEH and the proposed equivalent circuit modeling framework provide a practical design and analysis tool for optimizing real-world wind energy harvesters. In applications such as wireless sensor networks and autonomous monitoring stations, where energy reliability and low maintenance are critical, the findings from this study can guide the tailored design of harvesters and interface circuits. Future studies may focus on enhancing the SP-SECE circuit's efficiency under moderately or strongly coupled conditions. Compared to conventional VIV-based energy harvesters, the proposed VGPEH, with its ability to harness both VIV and galloping effects, offers enhanced performance at lower wind speeds. These advantages align with the practical requirements of compact, scalable, and robust wind energy harvesting systems for deployment in industries such as structural health monitoring, smart transportation infrastructure, and distributed sensing networks.

REFERENCES

[1] R. Parameshwaran, S. J. Dhulipalla, and D. R. Yendluri, "Fluid-structure interactions and flow induced vibrations: A review," in *Proc. Int. Conf. Vib. Problems*, Jan. 2016, vol. 144, pp. 1286–1293.
[2] S. Valtchev, J. Almeida, J. P. Teixeira, and J. B. Klaassens, "Conversion of wind-induced vibrations into electricity," in *Proc. IEEE 36th Int. Telecommun. Energy Conf.*, 2014, pp. 1–8.
[3] S. Francis and A. Swain, "Modelling and harnessing energy from flow-induced vibration, particularly VIV and galloping: An explicit review," *Ocean Eng.*, vol. 312, Nov. 2024, Art. no. 119290.
[4] M. J. Gong and B. Dally, "A review of flow-induced vibration in wind and oceanic flow: Mechanisms, applications, optimizations, and challenges," *Ocean Eng.*, vol. 325, May 2025, Art. no. 120748.
[5] S. Valtchev, J. Almeida, J. P. Teixeira, and J. Ben Klaassens, "Conversion of wind-induced vibrations into electricity," in *Proc. IEEE 36th Int. Telecommun. Energy Conf.*, Sep./Oct. 2014, pp. 1–8.
[6] N. Sezer and M. Koç, "A comprehensive review on the state-of-the-art of piezoelectric energy harvesting," *Nano Energy*, vol. 80, Feb, 2021, Art. no. 105567.
[7] D. Maurya et al., "Lead-free piezoelectric materials and composites for high power density energy harvesting," *J. Mater. Res.*, vol. 33, no. 16, pp. 2235–2263, 2018.
[8] J. T. Xing, M. Rezaei, H. L. Dai, and W. H. Liao, "Investigating the effect of surface protrusions on galloping energy harvesting," *Appl. Phys. Lett.*, vol. 122, no. 15, Apr. 2023, Art. no. 153902.

[9] H.-T. Li, H. Ren, F. Cao, and W.-Y. Qin, "Improving the galloping energy harvesting performance with magnetic coupling," *Int. J. Mech. Sci.*, vol. 237, 2023, Art. no. 107785.

[10] J. L. Wang et al., "Hybrid wind energy scavenging by coupling vortex-induced vibrations and galloping," *Energy Convers. Manage.*, vol. 213, Jun. 2020, Art. no. 112835.

[11] X. K. Yang, X. F. He, J. J. Li, and S. L. Jiang, "Modeling and verification of piezoelectric wind energy harvesters enhanced by interaction between vortex-induced vibration and galloping," *Smart Mater. Struct.*, vol. 28, no. 11, Nov. 2019, Art. no. 115027.

[12] D. Guyomar, A. Badel, E. Lefeuvre, and C. Richard, "Toward energy harvesting using active materials and conversion improvement by nonlinear processing," *IEEE/ASME Trans. Ultrason. Ferroelect. Freq. Control*, vol. 52, no. 4, pp. 584–595, Apr. 2005.

[13] E. Lefeuvre, A. Badel, C. Richard, and D. Guyomar, "Piezoelectric energy harvesting device optimization by synchronous electric charge extraction," *J. Intell. Mater. Syst. Struct.*, vol. 16, no. 10, pp. 865–876, Oct. 2005.

[14] H. K. Xia et al., "A self-powered S-SSHI and SECE hybrid rectifier for PE energy harvesters: Analysis and experiment," *IEEE Trans. Power Electron.*, vol. 36, no. 2, pp. 1680–1692, Feb. 2021.

[15] L. H. Tang, L. Y. Zhao, Y. W. Yang, and E. Lefeuvre, "Equivalent circuit representation and analysis of galloping-based wind energy harvesting," *IEEE/ASME Trans. Mechatron.*, vol. 20, no. 2, pp. 834–844, Apr. 2015.

[16] L. Zhao, L. Tang, J. Liang, and Y. Yang, "Synergy of wind energy harvesting and synchronized switch harvesting interface circuit," *IEEE/ASME Trans. Mechatron.*, vol. 22, no. 2, pp. 1093–1103, Apr. 2017.

[17] J. D. Jia, X. B. Shan, X. X. Zhang, T. Xie, and Y. W. Yang, "Equivalent circuit modeling and analysis of aerodynamic vortex-induced piezoelectric energy harvesting," *Smart Mater. Struct.*, vol. 31, no. 3, Mar. 2022, Art. no. 035009.

[18] E. D. Priore, G. P. Romano, and L. Lampani, "Coupled electro-aeroelastic energy harvester model based on piezoelectric transducers, VIV-galloping interaction and nonlinear switching circuits," *Smart Mater. Struct.*, vol. 32, no. 7, 2023, Art. no. 075012.

[19] J. L. Wang, L. J. Luo, D. Yurchenko, and G. B. Hu, "Equivalent circuit analysis of a nonlinear vortex-induced vibration piezoelectric energy harvester using synchronized switch technique," *IEEE/ASME Trans. Ind. Electron.*, vol. 72, no. 5, pp. 4865–4876, May 2025.

[20] C.-C. Chang, R. A. Kumar, and M. M. Bernitsas, "VIV and galloping of single circular cylinder with surface roughness at $3.0\times104\leq re\leq1.2\times105$," *Ocean Eng.*, vol. 38, no. 16, pp. 1713–1732, 2011.

[21] N. Y. Li, H. Park, H. Sun, and M. M. Bernitsas, "Hydrokinetic energy conversion using flow induced oscillations of single-cylinder with large passive turbulence control," *Appl. Energy*, vol. 308, Feb. 2022, Art. no. 118380.

[22] A. Vinod, A. Auvil, and A. Banerjee, "On passive control of transition to galloping of a circular cylinder undergoing vortex induced vibration using thick strips," *Ocean Eng.*, vol. 163, pp. 223–231, Sep. 2018.

[23] L. Ding, M. M. Bernitsas, and E. S. Kim, "2-D URANS vs. experiments of flow induced motions of two circular cylinders in tandem with passive turbulence control for $30{,}000<re<105{,}000$," *Ocean Eng.*, vol. 72, pp. 429–440, 2013.

[24] H. J. Li, M. M. Bernitsas, and H. Sun, "Interference effects on flow-induced oscillation of three tandem cylinders with passive turbulence control," *J. Offshore Mechan. Arctic Eng., Trans. ASME*, vol. 147, no. 2, Apr. 2025, Art. no. 021901.

[25] D. H. Zhang, H. Sun, W. H. Wang, and M. M. Bernitsas, "Rigid cylinder with asymmetric roughness in flow induced vibrations," *Ocean Eng.*, vol. 150, pp. 363–376, Feb. 2018.

[26] A. Abdelkefi, M. R. Hajj, and A. H. Nayfeh, "Power harvesting from transverse galloping of square cylinder," *Nonlinear Dyn.*, vol. 70, no. 2, pp. 1355–1363, Oct. 2012.

[27] P. Han et al., "Optimal energy harvesting efficiency from vortex-induced vibration of a circular cylinder," *Ocean Eng.*, vol. 282, Aug. 2023, Art. no. 114869.

[28] C. Mannini, T. Massai, A. M. Marra, and G. Bartoli, "Interference of vortex-induced vibration and galloping: Experiments and mathematical modelling," in *Proc. X Int. Conf. Struct. Dyn.*, vol. 199, 2017, pp. 3133–3138.

[29] A. Barrero-Gil, G. Alonso, and A. Sanz-Andres, "Energy harvesting from transverse galloping," *J. Sound Vib.*, vol. 329, no. 14, pp. 2873–2883, Jul. 2010.

[30] G. V. Parkinson and N. P. H. Brooks, "On the aeroelastic instability of bluff cylinders," *J. Appl. Mechan.*, vol. 28, no. 2, pp. 252–258, 1961.

[31] R. D. Blevins and W. D. Iwan, "The galloping response of a two-degree-of-freedom system," *J. Appl. Mechan.*, vol. 41, no. 4, pp. 1113–1118, 1974.

[32] A. Karimzadeh, M. Akbari, R. Roohi, and M. J. Amiri, "Dynamic behavior of galloping micro energy harvester with the elliptical bluff body using CFD simulation," *Sustainability*, vol. 15, no. 16, Aug. 2023, Art. no. 12187.

[33] Y. Tamura and G. Matsui, "Wake-oscillator model of vortex-induced vibration of circular cylinder," *Wind Eng.*, vol. 2, pp. 1085–1094, 1979.

[34] A. Naqvi, A. Ali, W. A. Altabey, and S. A. Kouritem, "Energy harvesting from fluid flow using piezoelectric materials: A review," *Energies*, vol. 15, no. 19, Oct. 2022, Art. no. 7424.

[35] M. P. Païdoussis, S. J. Price, and E. De Langre, *Fluid-structure Interactions: Cross-Flow-Induced Instabilities*. Cambridge, U.K.: Cambridge Univ. Press, 2010.

[36] C. H. K. Williamson and R. Govardhan, "Vortex-induced vibrations," *Annu. Rev. Fluid Mechan.*, vol. 36, no. 1, pp. 413–455, 2004.

[37] G. Q. Wang and Y. M. Lu, "An improved lumped parameter model for a piezoelectric energy harvester in transverse vibration," *Shock Vib.*, vol. 2014, pp. 1–12, 2014.

[38] L. Y. Zhao, L. H. Tang, and Y. W. Yang, "Comparison of modeling methods and parametric study for a piezoelectric wind energy harvester," *Smart Mater. Struct.*, vol. 22, no. 12, Dec. 2013, Art. no. 125003.

[39] M. Parsani, G. Ghorbaniasl, C. Lacor, and E. Turkel, "An implicit high-order spectral difference approach for large eddy simulation," *J. Comput. Phys.*, vol. 229, no. 14, pp. 5373–5393, Jul. 2010.

[40] J. L. Wang, S. X. Zhou, Z. E. Zhang, and D. Yurchenko, "High-performance piezoelectric wind energy harvester with Y-shaped attachments," *Energy Convers. Manage.*, vol. 181, pp. 645–652, Feb. 2019.

[41] Y. T. Ng, S. C. Luo, and Y. T. Chew, "On using high-order polynomial curve fits in the quasi-steady theory for square-cylinder galloping," *J. Fluids Struct.*, vol. 20, no. 1, pp. 141–146, Jan. 2005.

[42] L. Zhao, L. Tang, and Y. Yang, "Synchronized charge extraction in galloping piezoelectric energy harvesting," *J. Intell. Mater. Syst. Struct.*, vol. 27, no. 4, pp. 453–468, 2015.

[43] J. R. Liang and W. H. Liao, "Energy flow in piezoelectric energy harvesting systems," *Smart Mater. Struct.*, vol. 20, no. 1, Jan. 2011, Art. no. 015005.

[44] S. S. Sani, "A SP-SECE none-residual charge PEH interface circuit with an optimized phase delay," *IEEE Open J. Power Electron.*, vol. 6, pp. 712–733, 2025.

[45] X. Lv, H. Peng, J. Lei, Y. Zhao, and Y. Yan, "Phase delay analysis of SP-SECE for piezoelectric vibration energy harvesting and optimization," in *Proc. IEEE 10th Int. Power Electron. Motion Control Conf.*, 2024, pp. 4261–4266.

[46] L. H. Tang and Y. W. Yang, "Analysis of synchronized charge extraction for piezoelectric energy harvesting," *Smart Mater. Struct.*, vol. 20, no. 8, Aug. 2011, Art. no. 085022.

[47] D. Gibus et al., "Strongly coupled piezoelectric cantilevers for broadband vibration energy harvesting," *Appl. Energy*, vol. 277, Nov. 2020, Art. no. 115518.

[48] Y. Liao and H. Sodano, "Optimal power, power limit and damping of vibration based piezoelectric power harvesters," *Smart Mater. Struct.*, vol. 27, no. 7, 2018, Art. no. 075057.

[49] G. Hu, C. Lan, L. Tang, B. Zhou, and Y. Yang, "Dynamics and power limit analysis of a galloping piezoelectric energy harvester under forced excitation," *Mech. Syst. Signal Process.*, vol. 168, 2022, Art. no. 108724.

[50] E. Lefeuvre, A. Badel, A. Brenes, S. Seok, M. Woytasik, and C. S. Yoo, "Analysis of piezoelectric energy harvesting system with tunable SECE interface," *Smart Mater. Struct.*, vol. 26, no. 3, Mar. 2017, Art. no. 035065.

[51] J. L. Wang, B. Xia, D. Yurchenko, G. Litak, Y. Li, and H. G. Tian, "Enhanced performance of piezoelectric energy harvester by two asymmetrical splitter plates," *Ocean Eng.*, vol. 270, Feb. 2023, Art. no. 113614.

[52] W. Sun, Y. Zhang, G. G. Cheng, S. W. He, Z. R. Yang, and J. N. Ding, "An enhanced galloping-based piezoelectric energy harvester with non-rotational bluff body," *Appl. Phys. Lett.*, vol. 121, no. 17, Oct. 2022, Art. no. 173907.

[53] G. Hu, K. T. Tse, K. C. S. Kwok, J. Song, and Y. Lyu, "Aerodynamic modification to a circular cylinder to enhance the piezoelectric wind energy harvesting," *Appl. Phys. Lett.*, vol. 109, no. 19, Nov. 2016, Art. no. 193902.

[54] P. Poudel et al., "Enhancing the performance of piezoelectric wind energy harvester using curve-shaped attachments on the bluff body," *Glob. Challenges*, vol. 7, no. 4, Apr. 2023, Art. no. 2100140.

Ye Zhang received the B.E. degree in energy and power engineering from the Zhongyuan University of Technology, Zhengzhou, China, in 2021, and the M.E. degree in thermal engineering from Zhengzhou University, Zhengzhou, China, in 2024.

He is currently a Research Assistant with the Internet of Things Thrust, Information Hub, The Hong Kong University of Science and Technology (Guangzhou), Guangzhou, China. His research interests include flow-induced vibration energy harvesting, and flow-induced vibration control.

Yawei Wang received the M.E. degree in ocean engineering from Dalian Maritime University, Dalian, China, in 2023. He is currently working toward the doctoral degree in Internet of Things with The Hong Kong University of Science and Technology, Guangzhou, China.

His research interests include wave energy harvesting, battery-free monitoring systems, and triboelectric nanogenerators .

Junlei Wang received the B.E. and Ph.D. degrees in power and engineering thermosphysics from the School of Power Engineering, Chongqing University, Chongqing, China, in 2009 and 2014, respectively.

He is currently a Professor with the School of Mechanical and Power Engineering, Zhengzhou University, Zhengzhou, China. He was a Visiting Scholar in mechanical engineering with the University of Auckland, Auckland, New Zealand, from 2019 to 2020. His research interests include flow-induced vibration suppression, flow energy harvesting, and triboelectric, piezoelectric, and hybrid energy harvesting technologies.

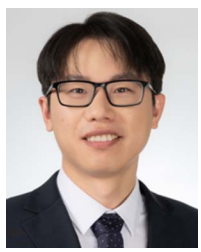

Guobiao Hu received the B.Eng. degree in mechanical engineering from Southwest Jiaotong University, Chengdu, China, in 2012, the Diplôme d'Ingénieur degree in general engineering from École Centrale Paris, Châtenay-Malabry, France, in 2015, and the Ph.D. degree in mechanical engineering from The University of Auckland, Auckland, New Zealand, in 2020.

He is currently a tenure-track Assistant Professor with the Internet of Things Thrust, Information Hub, The Hong Kong University of Science and Technology (Guangzhou), Guangzhou, China. His research interests include vibration/wind energy harvesting and acoustic–elastic metamaterials.